# First-Principles Ultrafast Exciton Dynamics and Time-Domain Spectroscopies

Hsiao-Yi Chen<sup>1, 2, 3</sup> and Marco Bernardi<sup>1, 2, \*</sup>

<sup>1</sup>Department of Applied Physics and Materials Science, California Institute of Technology, Pasadena, California 91125 <sup>2</sup>Department of Physics, California Institute of Technology, Pasadena, California 91125 <sup>3</sup>RIKEN Center for Emergent Matter Science (CEMS), Wako, Saitama, 351-0198, Japan

Electron-phonon (e-ph) interactions govern nonequilibrium dynamics and optical response in materials. Calculations combining first-principles e-ph interactions with the Boltzmann equation enable studies of ultrafast carrier and phonon dynamics. However, in materials with weak Coulomb screening, excitonic effects correlate the scattering processes of electrons and holes, posing new challenges for quantitative predictions of ultrafast dynamics. Here we show calculations of ultrafast exciton dynamics and related time-domain spectroscopies using ab initio exciton-phonon (ex-ph) interactions together with an excitonic Boltzmann equation. Starting from the nonequilibrium exciton populations, we develop calculations of time-domain absorption, photoemission and photoluminescence (PL) that take into account electron-hole correlations. The accuracy of the ex-ph interactions is validated by computing exciton linewidths and phonon-assisted PL. The methodology introduced in this work is general and enables studies of exciton dynamics and excitonic signatures in ultrafast spectroscopies in a wide range of materials.

## I. INTRODUCTION

First-principles approaches based on density functional theory (DFT) [1, 2] can characterize electronphonon (e-ph) interactions, enabling quantitative studies of nonequilibrium electron dynamics and transport
properties in materials ranging from semiconductors to
organic crystals and correlated electron systems [3–6].
However, these methods focus on the independent dynamics of electron and hole carriers, whereas in many
semiconductors, wide-gap insulators and nanostructured
materials, where the Coulomb interaction is weakly
screened, excited electrons and holes can form chargeneutral bound states (excitons) [7–9] which dominate the
optical response and light emission.

Although excitons cannot be easily manipulated with electric fields, controlling their diffusive dynamics is essential for efficient energy and lighting devices [10, 11], and trapping excitons in two-dimensional (2D) materials can provide stable optical qubits [12]. Excitons can additionally carry spin and valley quantum numbers, with potential applications to information storage and communication in spintronic and valleytronic devices [13–15]. Due to their robust excitonic effects persisting up to room temperature, 2D transition metal dichalcogenides (TMDs) have become a widely used platform for these exciton physics experiments [9, 16].

Time-domain optical and photoemission spectroscopies can probe the energy and internal structure of excitons, and characterize their interactions and dynamics down to the femtosecond time scale [8, 17–20]. Microscopic interpretation of these experiments is far from trivial, especially in cases where excitons are present. Therefore the development of theoretical methods to study ex-

citon dynamics and reveal excitonic signatures in timedomain spectra remains a priority. Several analytical or semiempirical models have been proposed to study exciton dynamics [21–23], but predictive first-principles calculations would be highly desirable to interpret and guide novel experiments in this rapidly evolving arena. Much first-principles work on excitons has focused on improving the description of their binding energy, optical response and radiative lifetime, typically using the GW-Bethe-Salpeter equation (GW-BSE) approach [24–29]. Combined with linear-response DFT, this framework has recently enabled the computation of ex-ph interactions and the associated phonon-induced exciton relaxation times and photoluminescence (PL) linewidths [30, 31]. This advance sets the stage for real-time simulations of exciton dynamics and time-domain spectroscopies.

Here we show calculations of ultrafast exciton dynamics based on exciton properties and ex-ph interactions computed from first principles with the Bethe-Salpeter equation (BSE). Our real-time simulations employ a bosonic Boltzmann transport equation (BTE) to evolve in time the exciton populations and characterize phonon-induced exciton relaxation. The exciton populations serve as input to predict time-resolved angleresolved photoemission (tr-ARPES) and transient absorption spectra including excitonic effects. We apply this method to monolayer WSe<sub>2</sub>, where our results reveal key ultrafast timescales for scattering of the photo excited bright exciton to indirect dark exciton states (400 fs) and phonon-induced valley depolarization following excitation with circularly polarized light (185 fs at 77 K and 65 fs at 300 K). Our work demonstrates a framework for quantitative studies of exciton dynamics and provides microscopic insight into exciton relaxation in 2D-TMDs.

<sup>\*</sup> bmarco@caltech.edu

#### II. RESULTS

#### A. Exciton band structure of monolayer WSe<sub>2</sub>

The effective mass approach has been widely used to model exciton dynamics [32, 33], but now one can compute the full exciton energy-momentum dispersion from first principles using the finite-momentum BSE [30, 34]. With this approach, we compute excitons in monolayer  $WSe_2$  with momenta  $\mathbf{Q}$  on a regular Brillouin zone (BZ) grid (see Appendix A). The resulting exciton band structure is shown in Fig. 1(a), where we highlight the energy of the lowest bright exciton,  $E_0 = 1.665$  eV, which is consistent with experiments [35]. This exciton band structure has two nearly-degenerate minima associated with a spin-singlet exciton at Q and a spin-triplet exciton at M, with the latter lower by 20 meV due to lack of exchange repulsion. As we focus on ex-ph interactions, using an average optical phonon frequency  $\omega_{\rm O} \approx 30 \text{ meV}$  in WSe<sub>2</sub>, we define a bright exciton relaxation window with energy  $E_0 \pm 60$  meV. In Fig. 1(b), we show the electronic transitions and the corresponding electron-hole pairs that primarily make up the excitons with momenta  $\mathbf{Q} = \mathbf{M}$ ,  $\mathbf{Q}$ , and K. For these excitons, the hole is located at the valence band edge at the K/K' BZ corner and the electron is at the conduction band minima at K or Q.

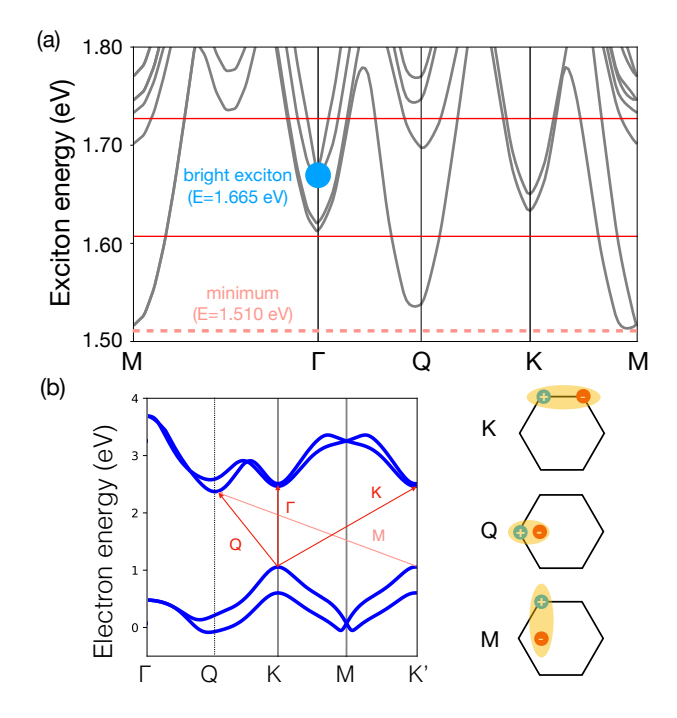


FIG. 1. (a) Exciton energy vs. momentum dispersion along high-symmetry lines, with minima at the M and Q points. The two lowest bright excitons are the  $3^{\rm rd}$  and  $4^{\rm th}$  states at  $\Gamma$ , with energy  $E_0=1.665$  eV as indicated with a blue dot. (b) Electronic band structure showing the transitions that make up excitons with  $\mathbf{Q}=(\mathbf{Q},\ \Gamma,\ \mathbf{M},\ \mathbf{K})$ . The corresponding electron-hole pairs are shown pictorially in the electronic BZ. The two lowest-energy excitons with  $\mathbf{Q}=(\mathbf{Q},\mathbf{M})$  correspond to indirect electronic transitions between the valence band maximum at K and the conduction band minimum at Q.

#### B. Photoluminescence linewidth

The PL linewidth in 2D-TMDs is a crucial indicator of material quality, and reflects intrinsic contributions due to radiative lifetime and ex-ph interactions, as well as extrinsic broadening from factors such as defects and substrate [32, 36–38]. Here we calculate the ex-ph interactions and validate their accuracy by computing the intrinsic PL linewidth due to ex-ph phonon interactions and comparing it with experiments.

To quantify the ex-ph interactions, we compute the exph matrix elements from the BSE exciton wave functions and e-ph interactions, with a procedure we developed in Ref. [30] (see Appendix A). The ex-ph matrix elements  $\mathcal{G}_{nm\nu}(\mathbf{Q}, \mathbf{q})$  describe the probability amplitude for an exciton in state  $|S_n(\mathbf{Q})\rangle$  to transition to state  $|S_m(\mathbf{Q}+\mathbf{q})\rangle$ when scattered by a phonon with mode  $\nu$  and momentum  $\mathbf{q}$ . We compute the intrinsic PL linewidth as the ex-ph lifetime of the lowest bright exciton [30, 39]:

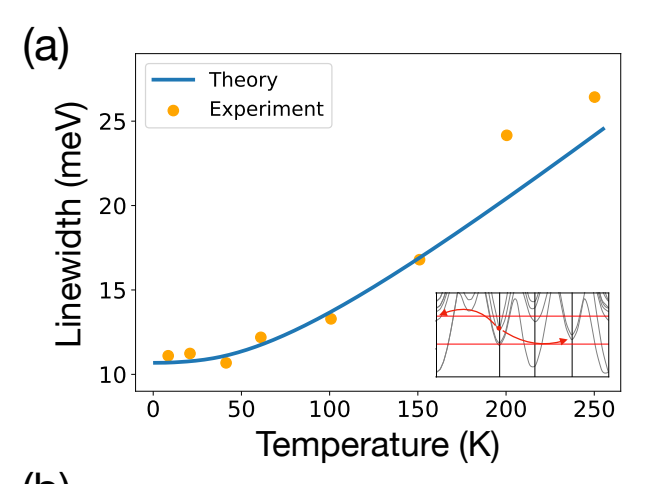
$$\Gamma(T) = \frac{2\pi}{N_{\mathbf{q}}} \sum_{m\nu\mathbf{q}} |\mathcal{G}_{n,m\nu}(\mathbf{Q}, \mathbf{q})|^{2}$$

$$\times \left[ (N_{\nu\mathbf{q}} + 1 + F_{m\mathbf{Q}+\mathbf{q}}) \times \delta(E_{n\mathbf{Q}} - E'_{m\mathbf{Q}+\mathbf{q}} - \hbar\omega_{\nu\mathbf{q}}) + (N_{\nu\mathbf{q}} - F_{m\mathbf{Q}+\mathbf{q}}) \times \delta(E_{n\mathbf{Q}} - E'_{m\mathbf{Q}+\mathbf{q}} + \hbar\omega_{\nu\mathbf{q}}) \right],$$
(1)

where  $\mathcal{N}_{\mathbf{q}}$  is the number of **q**-points in the BZ,  $E_{m\mathbf{Q}}$  is the exciton energy, and  $\omega_{\nu\mathbf{q}}$  is the phonon frequency;  $N_{\nu\mathbf{q}}$  is the thermal occupation number for phonons and  $F_{m\mathbf{Q}}$  for excitons, both satisfying the Bose-Einstein distribution at a given temperature T.

We focus on the lowest bright exciton, made up by an electron-hole pair in the K valley (corresponding to the  $|\mathbf{Q}| = 0, n = 3$  state in our BSE solution), which can recombine radiatively and emit circularly polarized light [14]. The temperature dependence of our computed PL linewidth, shown in Fig. 2(a), agrees closely with experiments from Ref. [38], although to match the experimental curve we need to apply a 7 meV rigid upward shift. We attribute this difference to temperature independent factors, including broadening from radiative decay and interactions with substrate and defects [36]. In the inset of Fig. 2(a), we highlight two key relaxation channels responsible for the linewidth, whereby the bright exciton gets scattered to the M-valley by phonon absorption or to the K-valley by phonon emission, consistent with recent experimental evidence [40].

We also analyze the phonon mode contributions to the linewidth. Previous work discussed the mode-dependent ex-ph interactions by symmetry analysis [41], but knowledge for generic phonon mode and momenta is still missing. In our framework, we can decompose the linewidth into contributions from different phonon modes and momenta. At low temperature (4 K), we find that both acoustic and optical phonons have significant contributions, with a linewidth ratio  $\Gamma^{\rm ac}/\Gamma^{\rm op}\approx 1.5$ . When the temperature is increased to 300 K, the acoustic phonons dominate exciton relaxation.



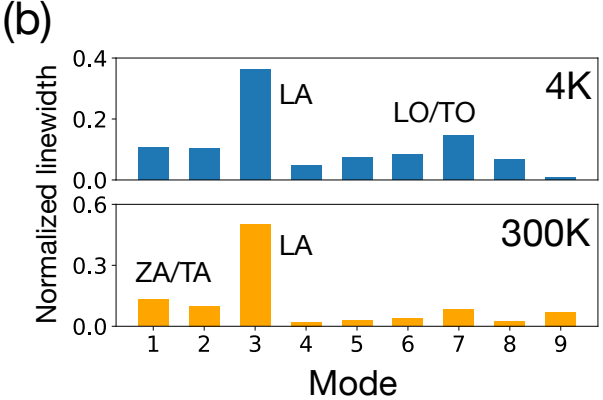


FIG. 2. (a) Computed PL linewidth from the lowest bright exciton, shown as a function of temperature and compared with experiment [38]. The inset shows two main ex-ph scattering processes for bright exciton relaxation,  $\Gamma$  to M and  $\Gamma$  to K. The computed results are shifted upward by  $\sim$ 7 meV to match experiment. (b) Contributions of different phonon modes to the PL linewidth given at two temperatures (4 K and 300 K). The values are normalized to the total linewidth at each temperature.

## C. Real-time exciton dynamics

We simulate real-time exciton dynamics using the exph interactions we discussed and validated above. Analogous to the case of electron dynamics [42, 43], we describe the exciton population dynamics using a real-time Boltzmann transport equation (rt-BTE) [42, 43]. The key difference from the standard formalism for e-ph scattering is that excitons follow the Bose-Einstein statistics [44]. Therefore, we derive a bosonic rt-BTE for exciton population dynamics:

$$\left(\frac{\partial F_{n\mathbf{Q}}}{\partial t}\right)^{\text{ex-ph}} = -\frac{2\pi}{\hbar} \frac{1}{\mathcal{N}_{\mathbf{q}}} \sum_{m\nu\mathbf{q}} \left| \mathcal{G}_{nm\nu}(\mathbf{Q}, \mathbf{q}) \right|^{2} 
\times \left[ \delta \left( E_{n\mathbf{Q}} - E_{m\mathbf{Q}+\mathbf{q}} + \hbar \omega_{\nu\mathbf{q}} \right) \cdot F_{\text{abs}}(t) \right] 
+ \delta \left( E_{n\mathbf{Q}} - E_{m\mathbf{Q}+\mathbf{q}} - \hbar \omega_{\nu\mathbf{q}} \right) \cdot F_{\text{em}}(t) \right].$$
(2)

The terms  $F_{\rm abs}(t)$  and  $F_{\rm em}(t)$  are occupation factors for absorption and emission processes, defined by extending

to excitons (treated as bosons) the corresponding equations for electrons [42, 43]:

$$F_{\text{abs}} = F_{n\mathbf{Q}} N_{\nu \mathbf{q}} (1 + F_{n\mathbf{Q}+\mathbf{q}})$$

$$- (1 + F_{n\mathbf{Q}}) (1 + N_{\nu \mathbf{q}}) F_{n\mathbf{Q}+\mathbf{q}}$$

$$F_{\text{em}} = F_{n\mathbf{Q}} (1 + N_{\nu \mathbf{q}}) (1 + F_{n\mathbf{Q}+\mathbf{q}})$$

$$- (1 + F_{n\mathbf{Q}}) N_{\nu \mathbf{q}} F_{n\mathbf{Q}+\mathbf{q}},$$
(3b)

where we suppress the time dependence of the exciton occupations,  $F_{n\mathbf{Q}}(t)$ , and assume constant phonon occupations  $N_{\nu\mathbf{q}}$  set to their thermal equilibrium value, a valid assumption in the low-excitation limit [42].

These occupation factors take into account the bosonic nature of excitons — for example, the first term in Eq. (3a) implies that the exciton population is unchanged by phonon absorption if the initial exciton state or the specific phonon mode are unoccupied ( $F_{n\mathbf{Q}} = 0$  or  $N_{\nu\mathbf{q}} = 0$ ). Conversely, the first term in Eq. (3b) describes the exciton population change during phonon emission, for which a finite phonon occupation is not required. In both equations, the second term accounts for the time reversal process of the respective first term, while the factors (1+F) reflect the exciton bosonic character and replace the (1-f) factor in e-ph scattering responsible for Pauli blocking [3].

The numerical calculations, carried out in the PER-TURBO code, employ a circularly polarized pump pulse at time zero with Gaussian shape in the time domain and a 50 fs full-width at half maximum. This pulse generates excitons in the lowest bright state consisting of electronhole pairs located at the K-point of the electronic BZ; the phonon distributions are kept to their thermal equilibrium value at 300 K. We time-step the exciton rt-BTE in Eq. (2) with an Euler algorithm using a 1 fs time step. In all discussions below, we measure time from the beginning of the pump pulse (with 50 fs width) which is taken as time t=0. Additional details are provided in Appendix A.

Snapshots of the exciton populations at times t = 30, 200, and 400 fs are shown in Fig. 3. At time t = 30 fs, when the circularly-polarized pump pulse is still on, the excitons reside primarily in the lowest bright exciton state at  $\Gamma$ , and a small fraction of excitons have transferred to the K-valley via intervalley scattering. An even smaller fraction of excitons absorb a phonon and scatter into exciton states at M with energy E=1.7 eV, or emit a phonon and transition to the Q-valley. In the t = 200fs panel in Fig. 3, after the pump has been turned off and excitons have relaxed more extensively, the chirality dependence becomes significant. Our initial excitation of the electronic K-valley results in a greater occupation of the exciton K- and Q'-valleys compared to the K'- and Qvalleys; the opposite trend is observed for a pump pulse with opposite-handed circular polarization. Finally, at time t = 400 fs time in Fig. 3(c), part of the excitons have relaxed to the global minima and the exciton populations at K and  $\Gamma$  are significantly reduced compared to their values at 200 fs; the Q'-valley has the highest occu-

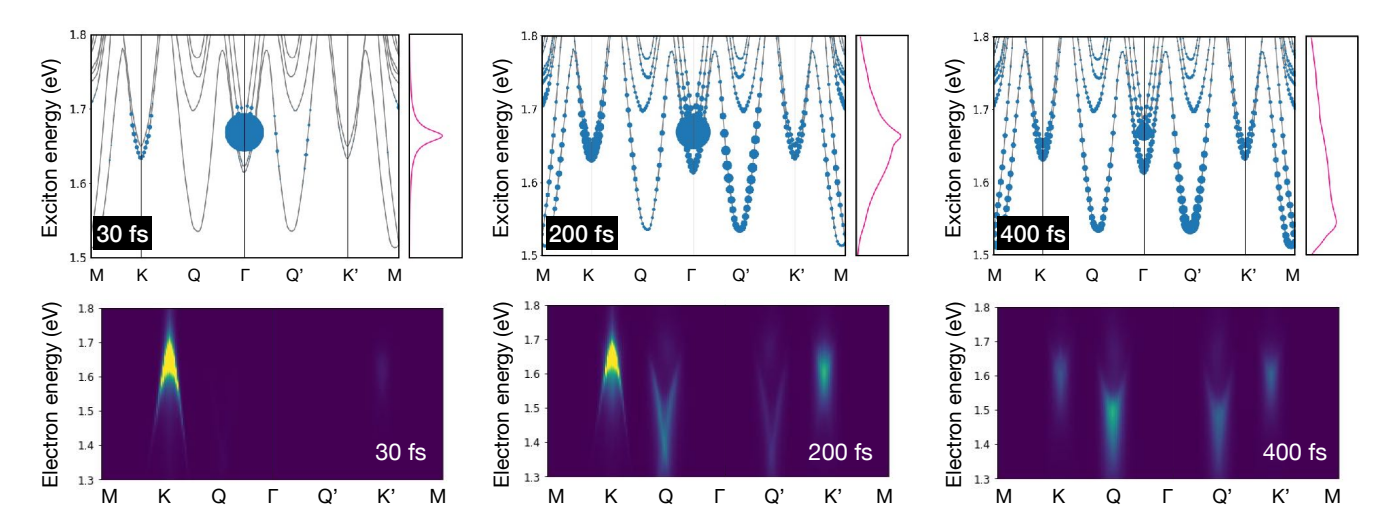


FIG. 3. Snapshots of exciton relaxation (top) and tr-ARPES spectra (bottom), shown at times t=30, 200, and 400 fs from left to right. The top panels map the exciton populations onto the exciton dispersion, with a spot radius proportional to the logarithm of the exciton populations,  $\log(F_{n\mathbf{Q}})$  in Eq. (2); next to each panel we give the energy-dependent exciton occupations g(E). The bottom panels show the corresponding electron distributions in simulated tr-ARPES spectra.

pation, but the number of M excitons is also increasing. These microscopic exciton relaxation pathways, accessed through our first-principles calculations, give rise to distinctive exciton signatures in time-domain spectra.

#### D. Simulated time-resolved ARPES

Recent experiments have shown that tr-ARPES is a valuable tool to study exciton dynamics owing to its ability to probe the time evolution of electron and hole carriers making up the exciton [45–47]. Similar to standard ARPES experiments, tr-ARPES measures the energy and momentum distribution of the photoemitted electrons, and additionally characterizes nonequilibrium dynamics with sub-ps time resolution [45]. The tr-ARPES signal  $I(\mathbf{k}, \omega; t)$  is the product of electron occupations  $f_a(\mathbf{k}; t)$ , for electronic state  $|a, \mathbf{k}\rangle$  at time t, and the corresponding spectral functions  $A_a(\mathbf{k}, \omega)$ . As the photoelectron is emitted from the bound exciton, one can relate the tr-ARPES signal to the exciton populations [48, 49]:

$$I(k,\omega;t) \propto \operatorname{Im}\left(\sum_{m\mathbf{Q}} F_{m\mathbf{Q}}(t) \sum_{cv} \frac{|A_{vc\mathbf{k}}^{m\mathbf{Q}}|^{2}}{\omega - (E_{m\mathbf{Q}} + \epsilon_{v\mathbf{Q}-\mathbf{k}}) + i\eta}\right), \quad (4)$$

where  $F_{m\mathbf{Q}}(t)$  are time-dependent exciton populations, obtained here from the rt-BTE, while the square exciton wave function  $|A_{cv\mathbf{k}}^{m\mathbf{Q}}|^2$  is the probability to find an electron, bound in the exciton state  $(m, \mathbf{Q})$ , at energy  $E_{m\mathbf{Q}} + \epsilon_{v\mathbf{Q}-\mathbf{k}}$ , where  $\epsilon_{v\mathbf{Q}-\mathbf{k}}$  is the hole energy (see Eq. (B2)); the broadening  $\eta$  is set to the exciton linewidth in Eq. (1). Based on this expression, the tr-ARPES signal is expected to exhibit a copy of the valence band shifted by the exciton energy-momentum dispersion  $E_{m\mathbf{Q}}$  and weighted by the exciton wave function.

The simulated tr-ARPES spectra, obtained by converting the rt-BTE exciton populations  $F_{mQ}(t)$  to photoemission signal using Eq. (4), are shown in the lower panels of Fig. 3 at three different times. During the pump pulse, electrons making up the bright excitons are localized in a small region of the electronic BZ near K as a result of the direct-gap transition. Similar to a previous model of tr-ARPES [50], at early time during the pump pulse (t = 30 fs) the simulated tr-ARPES signal shows a downward parabola resembling the electronic valence band. This is a signature of optically pumped excitons with vanishing center-of-mass momentum dominating the exciton populations in our rt-BTE. At time t = 200 fs, electrons start occupying the K'-valley with energy 10-50 meV below the bright-exciton signal at K. We additionally find electrons in the Q-valley deriving from Q'-excitons. Finally, at 400 fs the signal at K and K' is weak, and the signal at Q reveals an upward parabolic band with a broad minimum due to overlapping signals from the M, Q, and Q' excitons. These results show that the exciton populations from the rt-BTE can be employed directly to predict tr-ARPES spectra and aid their microscopic interpretation.

## E. Transient absorption

The redistribution of valence electrons modifies the optical response of a material. Following optical excitations, with electrons excited in the conduction band and holes in the valence band, Pauli exclusion hampers additional optical transitions, thus reducing the absorption coefficient. Transient absorption in the presence of excitons has been studied primarily using simple models for the exciton wave function and transition dipoles [51–53]. Here we aim to make quantitative predictions of excitonic transient absorption spectra, by combining exciton

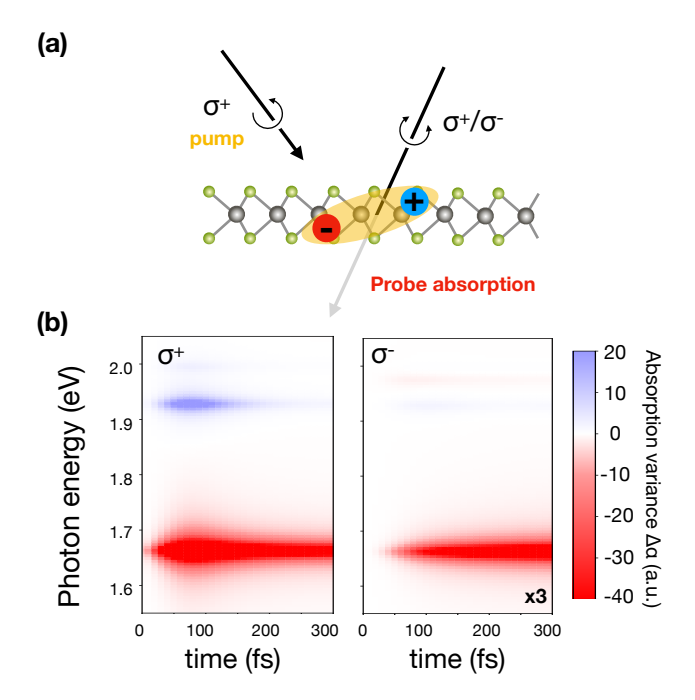


FIG. 4. (a) Schematic of our simulated pump-probe transient absorption settings. (b) Transient absorption spectra of monolayer WSe<sub>2</sub> pumped with a right-handed circularly polarized  $(\sigma^+)$  incident pulse. We plot separately the transient absorption spectra up to 300 fs for probes with  $\sigma^+$  (left panel) and  $\sigma^-$  (right panel) polarizations.

wave functions and transition dipoles from the *ab initio* BSE with time-domain exciton populations from our rt-BTE. We derive an expression for transient absorption that accounts for excitonic effects (see Appendix D):

$$\Delta\alpha(\omega, t) = -\frac{|\mathbf{p}_{n} \cdot \hat{\mathbf{e}}|^{2}}{\omega - E_{n} + i\gamma_{n}} \times \operatorname{Re}\left(\frac{\sum_{vc\mathbf{k}} (f_{c\mathbf{k}}(t) + f_{v\mathbf{k}}(t))(A_{vc\mathbf{k}}^{S_{n}} \mathbf{p}_{vc\mathbf{k}}) \cdot \hat{\mathbf{e}}}{\mathbf{p}_{n} \cdot \hat{\mathbf{e}}}\right), \quad (5)$$

where  $\mathbf{p}_n = \langle G|\mathbf{p}|S_n\rangle$  is the exciton transition dipole for the *n*-th excitonic state in the light-cone,  $\mathbf{p}_{vc\mathbf{k}} = \langle c\mathbf{k}|\mathbf{p}|v\mathbf{k}\rangle$  is the electronic transition dipole from the valence band v to the conduction band c at electronic wave vector  $\mathbf{k}$ , and  $\hat{\mathbf{e}}$  is the polarization of the probe. The electron and hole time-dependent occupations,  $f_{c\mathbf{k}}(t)$  and  $f_{v\mathbf{k}}(t)$  respectively, can be obtained from the exciton populations and the BSE exciton wave functions using:

$$f_{c\mathbf{k}}(t) = \sum_{m\mathbf{Q},v} F_{m\mathbf{Q}}(t) |A_{vc\mathbf{k}}^{S_m(\mathbf{Q})}|^2$$

$$f_{v\mathbf{k}}(t) = \sum_{m\mathbf{Q},c} F_{m\mathbf{Q}}(t) |A_{vc\mathbf{k}+\mathbf{Q}}^{S_m(\mathbf{Q})}|^2.$$
(6)

To study exciton relaxation, we use Eq. (5) with our rt-BTE exciton populations and study changes in the absorption coefficient for right-  $(\sigma^+)$  and left-handed  $(\sigma^-)$  circularly-polarized probe following a  $\sigma^+$  pump pulse, as

shown schematically in Fig. 4(a). The simulated transient absorption spectra, shown in the first 300 fs in Fig. 4(b), include signatures of exciton relaxation and intervalley scattering. For the  $\sigma^+$  probe, absorption of  $\sigma^+$  light is reduced near the bright-exciton resonance at  $\sim 1.665$  eV due to Pauli blocking; after the pump pulse is turned off, starting at 75 fs the absorption gradually increases toward the equilibrium value as excitons relax and thermalize.

Different from the independent-particle picture, where transient absorption due to Pauli blocking is always negative, the excitonic transient absorption in Eq. (5) can be both positive and negative. At higher energies of 1.93 and 1.98 eV, while the pump pulse is still on, we find positive transient absorption values due to an enhancement of the effective transition dipoles in the presence of finite exciton populations (see Appendix D). Conversely, for the  $\sigma^-$  probe, Pauli blocking plays only a minor role as the absorption of  $\sigma^-$  polarized light is in general weak when the pump pulse is  $\sigma^+$  polarized. In this case, the negative transient absorption is observed only after a 50 fs time delay after the  $\sigma^+$  pump is turned on  $(t=50~{\rm fs}$  in the right panel in Fig. 4(b)) and increase monotonically in time during our simulation.

#### F. Exciton depolarization

Due to spin-valley locking, electronic intervalley scattering from e-ph interactions is weak in 2D-TMDs, especially for hole carriers [41, 54] [To Marco: Yes, especially for electron. Consequently, the role of phonons in exciton depolarization has been largely ignored in previous work, with the exception of a recent study showing a significant contribution to intervalley spin-flip scattering from e-ph interactions [55]. To Marco: Yes, basically the Fig 6(c) in the paper (https://pubs.acs.org/doi/full/10.1021/acs.nanolett.8b02774) is our 5(b). This one is very good to support our computed hundreds fs time scale. But we don't need their data since the material is different. When excitons are taken into account, intervalley spin-flip processes can be mediated by intermediate dark exciton states without a well-defined spin character, opening up a broader phase space for intervalley scattering, as shown pictorially in Fig. 5(a).

We examine these bright-to-dark exciton scattering processes in detail using our exciton rt-BTE simulations, and compute phonon-induced exciton depolarization times using the exciton populations in the K- and K'-valleys. As we show in Fig. 5(b), the K-valley exciton population increases rapidly during the pump pulse (first 50 fs) and then decreases due to ex-ph scattering processes. Meanwhile, the K'-valley exciton population increases and peaks  $\sim 100$  fs after the K-valley exciton population has reached a maximum, after which it decreases very slowly, to about half of its peak value in the following 200 fs.

We quantify the exciton depolarization time by fitting

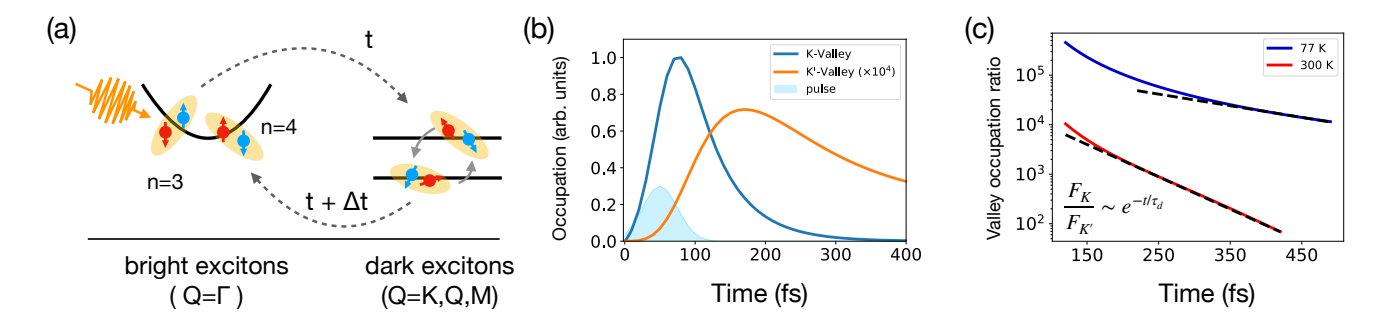


FIG. 5. Real-time simulation of exciton valley depolarization at  $T=300~\rm K$ . (a) Exciton populations in the K and K' valleys following a simulated  $\sigma^+$  pump pulse with Gaussian shape and 50 fs width. (b) Corresponding ratio of the K and K' valley occupations after the pump pulse. The depolarization times extracted from the simulation are  $\tau_{\rm d}=66~\rm fs$  at 300 K and  $\tau_{\rm d}=185~\rm fs$  at 77 K .

the ratio of the exciton populations in the two valleys:

$$\frac{F_{\rm K}}{F_{\rm K'}} = A \, e^{-(t-t_0)/\tau_{\rm d}} \tag{7}$$

where A and  $t_0$  are constants dependent on simulation settings such as pulse strength and pulse duration, and the time constant  $\tau_{\rm d}$  is the phonon-induced exciton depolarization time. In Fig. 5(c), fitting K and K'-valley occupation data between 170–420 fs, we obtain exciton depolarization times for monolayer WSe<sub>2</sub> of about  $\tau_d=185$  fs at 77 K and  $\tau_d=66$  fs at 300 K. Beyond 450 fs, excitons occupy equally the K and K' valleys, and the initial valley polarization is entirely lost.

To Marco: We should rewrite this part by referring more on the WS2 nano lett. I think, from the exp data, there are two relaxation/depolarization pattern, which are called  $\tau^{fast}$  and  $\tau^{slow}$ , while the former one is of  $\sim 100$  fs and the later id  $\sim 1$  ps. Our simulation is within 0.5 ps, thus gives the  $\tau^{fast}$ . On the other hand, the Zhu's paper, they fit the data to few ps scale, so that's should be  $\tau^{slow}$ . These results are compatible with the study on monolayer WS<sub>2</sub> [To Marco: Zhu's paper is on WSe<sub>2</sub>?] in Ref. [56], where the authors measured an exciton vallev depolarization time of 1.5 ps at 125 K that decreases rapidly with temperature above  $\sim 30$  K, in the regime discussed here where ex-ph interactions are important. The remaining  $\sim 10x$  difference of  $\tau_{\rm d}$  with experiment can be at least partially attributed to the  $SiO_2$  substrate used in Ref. [56] [To Marco: I think the major effect of the substrate is on the band structure, which can make the gap to a direct gap rather than the indirect one as we use, such that it has less scattering channel and takes longer time.], which screens the exciton interactions with polar optical phonons and slows down the ex-ph intervalley scattering. Our computed 185 fs exciton valley depolarization time at 77 K should be regarded as an intrinsic limit for suspended monolayer WSe<sub>2</sub>, within reasonable margins of error due to the choice of DFT, GW-BSE and ex-ph computational settings.

#### G. Phonon-assisted photoluminescence

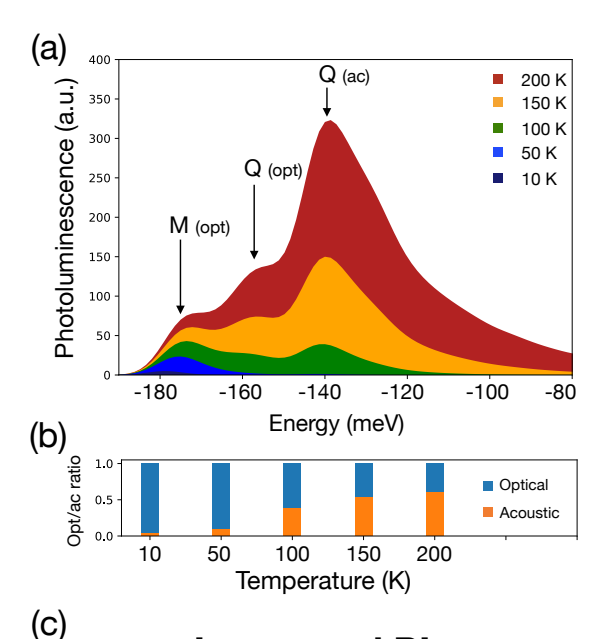
We conclude by analyzing the PL spectrum to clarify the interactions of dark excitons with phonons. These dark excitons possess a momentum  ${\bf Q}$  greater than the light-cone value,  $E_{\bf Q}/\hbar c$ , and as such they cannot recombine radiatively. Exciton-phonon interactions provide a pathway to circumvent this restriction — as phonons transfer momentum to the dark excitons, these can be scattered in the light cone and contribute to the PL [28, 57]. Therefore the PL spectrum encodes rich information on the energies and ex-ph coupling of dark excitons, particularly in materials with indirect gap like monolayer WSe<sub>2</sub>. The phonon-assisted PL contributions from dark excitons can be computed from the ex-ph interactions, using a formula we recently derived [30]:

$$I(\omega) \propto \sum_{nm\nu} |\hat{\mathbf{e}} \cdot \mathbf{p}_{S_m}|^2 \int d\mathbf{Q} |\mathcal{G}_{nm\nu}(\mathbf{Q}, -\mathbf{Q})|^2$$

$$\times N_n \mathbf{Q} \frac{1 + N(\hbar\omega)}{(\hbar\omega - E_m)^2} \cdot \delta(\hbar\omega + \hbar\omega_{\nu\mathbf{Q}} - E_{n\mathbf{Q}}), \qquad (8)$$

where  $\omega$  is the PL frequency,  $\hat{\mathbf{e}}$  is the polarization of the emitted photon and  $\mathbf{p}_{S_m}$  is the transition dipole of the exciton in state  $S_m$ .

We focus on circularly polarized PL by choosing  $\hat{\mathbf{e}} = (1, i, 0)$ . The predicted PL spectrum from 10-200K in Fig. 6(a), where the PL frequency is referenced to the bright-exciton energy. We find three main emission peaks, respectively 175 meV, 158 meV, and 140 meV below the bright exciton energy. For temperatures below 50 K, the PL is dominated by the exciton in the global minimum at the M-point. Although this exciton is a spin-triplet, the occupation factor in Eq. (8) suppresses the contribution from the spin-singlet exciton at the Q-point, which is 20 meV higher in energy. Our analysis in Fig. 6(b) shows that at low temperature ex-ph scattering from optical phonons governs the PL spectrum. This result is in contrast with the calculation in Ref. [33], where the low-temperature PL is shown to be dominated by acoustic phonon emission. attribute this difference to the electronic structure used in Ref. [33], where WSe<sub>2</sub> is treated as a direct gap



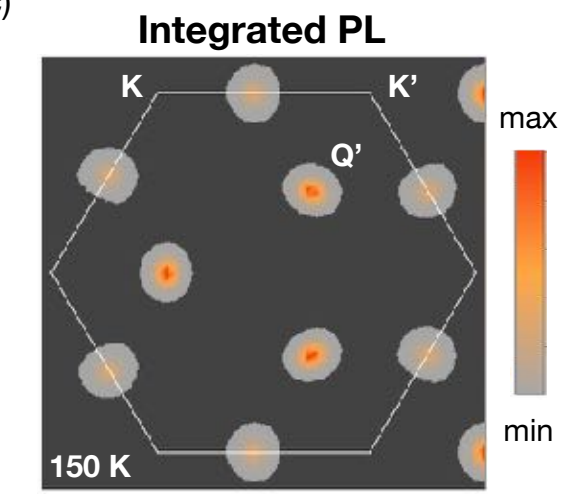


FIG. 6. (a) Theoretical prediction of the phonon-assisted PL between  $10-200~\rm K$ . The bright exciton energy is set as the energy zero. (b) Ratio of the phonon-assisted PL contributions from optical and acoustic phonons shown at different temperatures. (c) Exciton-momentum resolved contribution to the PL intensity. The most intense peaks, forming a pattern with three-fold symmetry, are from excitons with Q' momentum.

material whereas in this work the electronic band gap is indirect. Although the precise location of the conduction band minimum is still under debate, growing evidence points to the indirect gap nature of WSe<sub>2</sub> [58].

At higher temperatures, the higher-energy spin-singlet exciton at the Q-point comes into play - above 100 K, the dominant PL signal comes from this Q-exciton emitting an acoustic phonon with 140 meV energy, and the second-strongest comes from the emission of an optical phonon with 158 meV energy. These processes are associated with PL peaks, respectively, at 140 meV and 158 meV below the bright exciton energy in Fig. 6(a). We also observe an overall increasing contribution to the PL from acoustic phonons over optical phonons at increasing temperatures [Fig. 6(b)]. The momentumresolved contribution to the PL from dark excitons is shown in Fig. 6(c) as a color map in the exciton BZ. This plot shows that excitons with Q' momentum are primarily responsible for the phonon-assisted PL at 150 K, with a smaller contribution from excitons at M. Our phonon-mode and exciton-momentum resolved maps reveal the microscopic origin of the PL.

#### III. SUMMARY

We presented an approach to study exciton dynamics using accurate ex-ph interactions computed from first principles. Our method is based on a bosonic Boltzmann equation that leverages material-specific exciton quantities from the ab initio BSE, thus going beyond heuristic models of exciton dynamics. Simulation of real-time exciton dynamics in monolayer WSe<sub>2</sub> reveal the main pathways for phonon-induced exciton relaxation and valley depolarization mediated by dark excitons, leading to quantitative predictions of sub-ps exciton valley depolarization times. These results provide a detailed picture of exciton motion in a 2D-TMDs and enable the simulation of state-of-the-art ultrafast probes of excitons dynamics, including transient absorption and tr-ARPES spectra, in both cases going beyond the single-particle picture and properly capturing excitonic effects. Although the current formalism does not treat time-domain lattice dynamics and nonlinear optical effects, this physics can also be addressed by extending our formalism. Taken together, this work paves the way for quantitative studies of exciton dynamics and the related time-domain spectroscopies for several classes of materials with strongly bound exictons.

## ACKNOWLEDGMENTS

The authors thank Davide Sangalli and Ivan Maliyov for fruitful discussions. This material is based upon work supported by the U.S. Department of Energy, Office of Science, Office of Advanced Scientific Computing Research and Office of Basic Energy Sciences, Scientific Discovery through Advanced Computing (SciDAC) program under Award Number DE-SC0022088, which

supported method development. Code development was partially supported by the National Science Foundation under Grant No. OAC-2209262. H.-Y. Chen was partially supported by the J. Yang Fellowship. This research used resources of the National Energy Research Scientific Computing Center (NERSC), a U.S. Department of Energy Office of Science User Facility located at Lawrence Berkeley National Laboratory, operated under Contract No. DE-AC02-05CH11231.

## Appendix A: Computational details

The DFT calculations on monolayer WSe<sub>2</sub> are carried out using a relaxed lattice constant of 3.27 A and a 20 Å layer-normal separation between periodic replicas. The ground state is computed using DFT in the generalized gradient approximation with the QUANTUM Espresso code [59]. We employ a 60 Ry kinetic energy cutoff to compute the electronic structure on a  $72 \times 72 \times 1$ regular k-point grid in the BZ. The lattice dynamics and e-ph perturbation potentials are computed with density functional perturbation theory [2] on a  $36 \times 36 \times 1$  phonon momentum q-grid using QUANTUM ESPRESSO. We use the Perturbo code [60] to compute the e-ph matrix elements on these electron and phonon momentum grids. All calculations include spin-orbit coupling by using fully relativistic norm-conserving pseudopotentials generated with Pseudo Dojo [61–63].

## Appendix B: Bethe-Salpeter equation

The first-principles BSE calculations solve the effective exciton Hamiltonian [24]

$$H_{vc,v'c'} = \langle vc|H|v'c'\rangle = (\epsilon_c - \epsilon_v)\delta_{vv'}\delta_{cc'} + K_{vc,v'c'}$$
 (B1)

with kernel  $K_{vc,v'c'}$  describing the electron-hole interactions. The solutions provide the exciton energies  $E_S$  and the wave functions  $|S\rangle$  expressed in the transition basis, with expansion coefficients  $A_{vck}^S$  satisfying [24]:

$$\sum_{c'v'\mathbf{k}'} H_{vc\mathbf{k},v'c'\mathbf{k}'} A_{v'c'\mathbf{k}'}^S = E_S A_{vc\mathbf{k}}^S$$

$$|S\rangle = \sum_{vc\mathbf{k}} A_{vc\mathbf{k}}^S |cv\mathbf{k}\rangle, \tag{B2}$$

where v and c are valence and conduction band indices, and  $\epsilon_v$  and  $\epsilon_c$  are the corresponding quasiparticle energies. The finite-momentum BSE calculations presented in this work are carried out with the YAMBO code [64]. The screened Coulomb interaction is computed using a 5 Ry cutoff and 300 bands. To construct the BSE Hamiltonian, we fine-tune the electronic band structure to reproduce the experimental band gap and the relative valley energies [58]; we use the 2 highest valence bands and 4 lowest conduction bands together with a 30 Ry cutoff for the exchange and a 4 Ry cutoff for the correlation parts of the BSE kernel. These calculations are carried out on a  $36 \times 36 \times 1$  exciton momentum **Q**-grid without using symmetry.

## Appendix C: Exciton dynamics

We implement the exciton rt-BTE in a developer version of our PERTURBO code. The ex-ph matrix element elements  $\mathcal{G}_{nm\nu}(\mathbf{Q}, \mathbf{q})$  used in the rt-BTE, which quantify the coupling strength between excitons and phonons as discussed above, are computed by combining first-principles BSE and e-ph calculations [30]. In this work,

the ex-ph matrix elements are computed directly on a  $36 \times 36 \times 1$  regular grid for both phonon and exciton momenta. For the rt-BTE and PL calculations, we use linear interpolation to obtain the ex-ph matrix elements and exciton energies on  $216 \times 216 \times 1$  **q**- and **Q**-point grids. The real-time simulations are performed on this grid using the 10 lowest exciton bands.

## Appendix D: Excitonic transient absorption

We derive the transient absorption formula, Eq. (5), by extending the model in Ref. [53] to the *ab initio* BSE formalism. In the presence of photoexcited carrier, the exciton wave function follows the transition-basis expansion under the modulation of Pauli exclusion:

$$|S_n\rangle = \sum_{vc\mathbf{k}} A_{vc\mathbf{k}}^{S_n} (1 - f_{c\mathbf{k}} - f_{v\mathbf{k}})^{1/2} |\mathbf{k}, c\rangle |\mathbf{k}, v\rangle \qquad (D1)$$

where  $f_{c\mathbf{k}}$  are electron and  $f_{v\mathbf{k}}$  hole populations. The corresponding exciton transition dipole becomes

$$\tilde{\mathbf{p}}_n = \sum_{vc\mathbf{k}} A_{vc\mathbf{k}}^{S_n} (1 - f_{c\mathbf{k}} - f_{v\mathbf{k}})^{1/2} \mathbf{p}_{vc\mathbf{k}}, \quad (D2)$$

where  $\tilde{\mathbf{p}}_n$  denotes the dipole modulated by the carrier populations (as opposed to the intrinsic dipole,  $\mathbf{p}_n$ ).

For incident light with frequency  $\omega$  and polarization  $\hat{\mathbf{e}}$ , we define the change of exciton absorption due to the

finite-carrier populations as

$$\Delta\alpha(\omega) = \sum_{n} \frac{|(\tilde{\mathbf{p}}_{n} - \mathbf{p}_{n}) \cdot \hat{\mathbf{e}}|^{2}}{\omega - E_{n} + i\gamma_{n}}$$
(D3)

Expanding terms proportional to the electron/hole populations to lowest order, we obtain

$$|\tilde{\mathbf{p}}_{n} \cdot \hat{\mathbf{e}}|^{2} = \left| \sum_{vc\mathbf{k}} A_{vc\mathbf{k}}^{S_{n}} (1 - f_{c\mathbf{k}} - f_{v\mathbf{k}})^{1/2} \mathbf{p}_{vc\mathbf{k}} \cdot \hat{\mathbf{e}} \right|^{2}$$

$$\approx \left| \sum_{vc\mathbf{k}} A_{vc\mathbf{k}}^{S_{n}} \mathbf{p}_{vc\mathbf{k}} \cdot \hat{\mathbf{e}} - \sum_{vc\mathbf{k}} (\frac{f_{c\mathbf{k}} + f_{v\mathbf{k}}}{2}) A_{vc\mathbf{k}}^{S_{n}} \mathbf{p}_{vc\mathbf{k}} \cdot \hat{\mathbf{e}} \right|^{2}$$

$$= |\mathbf{p}_{n} \cdot \hat{\mathbf{e}}|^{2} \left| 1 - \left( \frac{\sum_{vc\mathbf{k}} (f_{c\mathbf{k}} + f_{v\mathbf{k}}) (A_{vc\mathbf{k}}^{S_{n}} \mathbf{p}_{vc\mathbf{k}}) \cdot \hat{\mathbf{e}}}{2 \mathbf{p}_{n} \cdot \hat{\mathbf{e}}} \right) \right|^{2}$$

$$\approx |\mathbf{p}_{n} \cdot \hat{\mathbf{e}}|^{2} \left[ 1 - \operatorname{Re} \left( \frac{\sum_{vc\mathbf{k}} (f_{c\mathbf{k}} + f_{v\mathbf{k}}) (A_{vc\mathbf{k}}^{S_{n}} \mathbf{p}_{vc\mathbf{k}}) \cdot \hat{\mathbf{e}}}{\mathbf{p}_{n} \cdot \hat{\mathbf{e}}} \right) \right]. \tag{D4}$$

Thus we obtain the final result used in Eq. (5):

$$\Delta\alpha(\omega) = -\sum_{n} \frac{|\mathbf{p}_{n} \cdot \hat{\mathbf{e}}|^{2}}{\omega - E_{n} + i\gamma_{n}} \times \operatorname{Re}\left(\frac{\sum_{vc\mathbf{k}} (f_{c\mathbf{k}} + f_{v\mathbf{k}})(A_{vc\mathbf{k}}^{S_{n}} \mathbf{p}_{vc\mathbf{k}}) \cdot \hat{\mathbf{e}}}{\mathbf{p}_{n} \cdot \hat{\mathbf{e}}}\right). \tag{D5}$$

- [1] R. M. Martin, Electronic Structure: Basic Theory and Practical Methods (Cambridge University Press, 2020).
- [2] S. Baroni, S. De Gironcoli, A. Dal Corso, and P. Giannozzi, Rev. Mod. Phys. 73, 515 (2001).
- [3] M. Bernardi, Eur. Phys. J. B 89, 239 (2016).
- [4] J.-J. Zhou and M. Bernardi, Phys. Rev. B 94, 201201 (2016).
- [5] N.-E. Lee, J.-J. Zhou, L. A. Agapito, and M. Bernardi, Phys. Rev. B 97, 115203 (2018).
- [6] J.-J. Zhou, J. Park, I. Timrov, A. Floris, M. Cococcioni, N. Marzari, and M. Bernardi, Phys. Rev. Lett. 127, 126404 (2021).
- [7] R. S. Knox, Theory of Excitons (Solid State Phys. Suppl. 5), Vol. 5 (Academic Press, New York, 1963).
- [8] G. Wang, A. Chernikov, M. M. Glazov, T. F. Heinz, X. Marie, T. Amand, and B. Urbaszek, Rev. Mod. Phys. 90, 021001 (2018).
- [9] T. Mueller and E. Malic, npj 2D Mater. Appl. 2, 1 (2018).
- [10] B. A. Gregg, J. Phys. Chem. B **107**, 4688 (2003).
- [11] S. M. Menke and R. J. Holmes, Energy Environ. Sci. 7, 499 (2014).
- [12] D. Thureja, A. Imamoglu, T. Smoleński, I. Amelio, A. Popert, T. Chervy, X. Lu, S. Liu, K. Barmak, K. Watanabe, et al., Nature 606, 298 (2022).
- [13] O. Gunawan, Y. P. Shkolnikov, K. Vakili, T. Gokmen, E. P. De Poortere, and M. Shayegan, Phys. Rev. Lett. 97, 186404 (2006).

- [14] D. Xiao, W. Yao, and Q. Niu, Phys. Rev. Lett. 99, 236809 (2007).
- [15] J. R. Schaibley, H. Yu, G. Clark, P. Rivera, J. S. Ross, K. L. Seyler, W. Yao, and X. Xu, Nat. Rev. Mater. 1, 1 (2016)
- [16] A. Tartakovskii, Nat. Rev. Phys. 2, 8 (2020).
- [17] R. Bertoni, C. W. Nicholson, L. Waldecker, H. Hübener, C. Monney, U. De Giovannini, M. Puppin, M. Hoesch, E. Springate, R. T. Chapman, C. Cacho, M. Wolf, A. Rubio, and R. Ernstorfer, Phys. Rev. Lett. 117, 277201 (2016).
- [18] J. Madéo, M. K. Man, C. Sahoo, M. Campbell, V. Pareek, E. L. Wong, A. Al-Mahboob, N. S. Chan, A. Karmakar, B. M. K. Mariserla, et al., Science 370, 1199 (2020).
- [19] M. Cho, H. M. Vaswani, T. Brixner, J. Stenger, and G. R. Fleming, J. Phys. Chem. B 109, 10542 (2005).
- [20] A. Rustagi and A. F. Kemper, Phys. Rev. B 97, 235310 (2018).
- [21] Y. Toyozawa, Prog. Theor. Phys. **20**, 53 (1958).
- [22] Y. Toyozawa, J. Phys. Chem. Solids **25**, 59 (1964).
- [23] B. Segall and G. D. Mahan, Phys. Rev. 171, 935 (1968).
- [24] M. Rohlfing and S. G. Louie, Phys. Rev. B 62, 4927 (2000).
- [25] G. Onida, L. Reining, and A. Rubio, Rev. Mod. Phys. 74, 601 (2002).

- [26] C. D. Spataru, S. Ismail-Beigi, L. X. Benedict, and S. G. Louie, Phys. Rev. Lett. 92, 077402 (2004).
- [27] M. Palummo, M. Bernardi, and J. C. Grossman, Nano Lett. 15, 2794 (2015).
- [28] H.-Y. Chen, M. Palummo, D. Sangalli, and M. Bernardi, Nano Lett. 18, 3839 (2018).
- [29] V. A. Jhalani, H.-Y. Chen, M. Palummo, and M. Bernardi, J. Phys. Condens. Matter 32, 084001 (2019).
- [30] H.-Y. Chen, D. Sangalli, and M. Bernardi, Phys. Rev. Lett. 125, 107401 (2020).
- [31] G. Antonius and S. G. Louie, Phys. Rev. B 105, 085111 (2022).
- [32] M. Selig, G. Berghäuser, A. Raja, P. Nagler, C. Schüller, T. F. Heinz, T. Korn, A. Chernikov, E. Malic, and A. Knorr, Nat. Commun. 7, 1 (2016).
- [33] S. Brem, A. Ekman, D. Christiansen, F. Katsch, M. Selig, C. Robert, X. Marie, B. Urbaszek, A. Knorr, and E. Malic, Nano Lett. 20, 2849 (2020).
- [34] L. Sponza, H. Amara, C. Attaccalite, S. Latil, T. Galvani, F. Paleari, L. Wirtz, and F. Ducastelle, Phys. Rev. B 98, 125206 (2018).
- [35] S. Mouri, Y. Miyauchi, M. Toh, W. Zhao, G. Eda, and K. Matsuda, Phys. Rev. B 90, 155449 (2014).
- [36] O. A. Ajayi, J. V. Ardelean, G. D. Shepard, J. Wang, A. Antony, T. Taniguchi, K. Watanabe, T. F. Heinz, S. Strauf, X.-Y. Zhu, and J. C. Hone, 2D Mater. 4, 031011 (2017).
- [37] G. Moody, C. K. Dass, K. Hao, C.-H. Chen, L.-J. Li, A. Singh, K. Tran, G. Clark, X. Xu, G. Berghäuser, et al., Nat. Commun. 6, 1 (2015).
- [38] V. Chellappan, A. L. C. Pang, S. Sarkar, Z. E. Ooi, and K. E. J. Goh, Electron. Mater. Lett. 14, 766 (2018).
- [39] M. Kira and S. W. Koch, Prog. Quantum Electron. 30, 155 (2006).
- [40] H. Liu, J. Chen, H. Yu, F. Yang, L. Jiao, G.-B. Liu, W. Ho, C. Gao, J. Jia, W. Yao, and M. Xie, Nat. Commun. 6, 1 (2015).
- [41] M. He, P. Rivera, D. Van Tuan, N. P. Wilson, M. Yang, T. Taniguchi, K. Watanabe, J. Yan, D. G. Mandrus, H. Yu, H. Dery, W. Yao, and X. Xu, Nat. Commun. 11, 1 (2020).
- [42] V. A. Jhalani, J.-J. Zhou, and M. Bernardi, Nano Lett. 17, 5012 (2017).
- [43] X. Tong and M. Bernardi, Phys. Rev. Research 3, 023072 (2021).
- [44] D. W. Snoke, *Solid State Physics: Essential Concepts* (Cambridge University Press, 2020).
- [45] E. J. Sie, T. Rohwer, C. Lee, and N. Gedik, Nat. Commun. 10, 1 (2019).
- [46] J. Madéo, M. K. Man, C. Sahoo, M. Campbell, V. Pareek, E. L. Wong, A. Al-Mahboob, N. S. Chan, A. Karmakar, B. M. K. Mariserla, et al., Science 370, 1199 (2020).

- [47] M. K. L. Man, J. Madéo, C. Sahoo, K. Xie, M. Campbell, V. Pareek, A. Karmakar, E. L. Wong, A. Al-Mahboob, N. S. Chan, D. R. Bacon, X. Zhu, M. M. M. Abdelrasoul, X. Li, T. F. Heinz, F. H. da Jornada, T. Cao, and K. M. Dani, Sci. Adv. 7, eabg0192 (2021).
- [48] E. Perfetto, D. Sangalli, A. Marini, and G. Stefanucci, Phys. Rev. B 94, 245303 (2016).
- [49] D. Sangalli, Phys. Rev. Materials 5, 083803 (2021).
- [50] D. Christiansen, M. Selig, E. Malic, R. Ernstorfer, and A. Knorr, Phys. Rev. B 100, 205401 (2019).
- [51] M. Shinada and S. Sugano, J. Phys. Soc. Japan 21, 1936 (1966).
- [52] S. Schmitt-Rink, D. S. Chemla, and D. A. B. Miller, Phys. Rev. B 32, 6601 (1985).
- [53] D. Huang, J.-I. Chyi, and H. Morkoç, Phys. Rev. B 42, 5147 (1990).
- [54] D. Xiao, G.-B. Liu, W. Feng, X. Xu, and W. Yao, Phys. Rev. Lett. 108, 196802 (2012).
- [55] Z. Wang, A. Molina-Sánchez, P. Altmann, D. Sangalli, D. De Fazio, G. Soavi, U. Sassi, F. Bottegoni, F. Ciccacci, M. Finazzi, L. Wirtz, A. C. Ferrari, A. Marini, G. Cerullo, and S. Dal Conte, Nano Lett. 18, 6882 (2018).
- [56] C. R. Zhu, K. Zhang, M. Glazov, B. Urbaszek, T. Amand, Z. W. Ji, B. L. Liu, and X. Marie, Phys. Rev. B 90 (2014).
- [57] G. Cassabois, P. Valvin, and B. Gil, Nat. Photonics 10, 262 (2016).
- [58] C. Zhang, Y. Chen, A. Johnson, M.-Y. Li, L.-J. Li, P. C. Mende, R. M. Feenstra, and C.-K. Shih, Nano Lett. 15, 6494 (2015).
- [59] P. Giannozzi, S. Baroni, N. Bonini, M. Calandra, R. Car, C. Cavazzoni, D. Ceresoli, G. L. Chiarotti, M. Cococcioni, I. Dabo, A. D. Corso, S. de Gironcoli, S. Fabris, G. Fratesi, R. Gebauer, U. Gerstmann, C. Gougoussis, A. Kokalj, M. Lazzeri, L. Martin-Samos, N. Marzari, F. Mauri, R. Mazzarello, S. Paolini, A. Pasquarello, L. Paulatto, C. Sbraccia, S. Scandolo, G. Sclauzero, A. P. Seitsonen, A. Smogunov, P. Umari, and R. M. Wentzcovitch, J. Phys. Condens. Matter 21, 395502 (2009).
- [60] J.-J. Zhou, J. Park, I.-T. Lu, I. Maliyov, X. Tong, and M. Bernardi, Comput. Phys. Commun. 264, 107970 (2021).
- [61] J. P. Perdew and A. Zunger, Phys. Rev. B 23, 5048 (1981).
- [62] N. Troullier and J. L. Martins, Phys. Rev. B 43, 1993 (1991).
- [63] M. Van Setten, M. Giantomassi, E. Bousquet, M. J. Verstraete, D. R. Hamann, X. Gonze, and G.-M. Rignanese, Comput. Phys. Commun. 226, 39 (2018).
- [64] D. Sangalli, A. Ferretti, H. Miranda, C. Attaccalite, I. Marri, E. Cannuccia, P. Melo, M. Marsili, F. Paleari, A. Marrazzo, G. Prandini, P. Bonfà, M. O. Atambo, F. Affinito, M. Palummo, A. Molina-Sánchez, C. Hogan, M. Grüning, D. Varsano, and A. Marini, J. Phys. Condens. Matter 31, 325902 (2019).